RMetS
Royal Meteorological Society

Initiation of convection over the Black Forest mountains during COPS IOP15a

Lindsay J. Bennett,[a]* Alan M. Blyth,[b] Ralph R. Burton,[b] Alan M. Gadian,[b] Tammy M. Weckwerth,[c] Andreas Behrendt,[d] Paolo Di Girolamo,[e] Manfred Dorninger,[f] Sarah-Jane Lock,[a] Victoria H. Smith[a] and Stephen D. Mobbs[b]

[a]*Institute for Climate and Atmospheric Science, School of Earth and Environment, University of Leeds, Leeds, UK*
[b]*National Centre for Atmospheric Science and Institute for Climate and Atmospheric Science, School of Earth and Environment, University of Leeds, Leeds, UK*
[c]*Earth Observing Laboratory, National Center for Atmospheric Research, Boulder, USA*
[d]*Institut für Physik und Meteorologie, Universität Hohenheim, Stuttgart, Germany*
[e]*DIFA –Università degli Studi della Basilicata, Potenza, Italy*
[f]*Institut für Meteorologie und Geophysik, Universität Wien, Austria*
*Correspondence to: Lindsay J. Bennett, Institute for Climate and Atmospheric Science, School of Earth and Environment, University of Leeds, Leeds, LS2 9JT, UK. E-mail: l.j.bennett@leeds.ac.uk

Doppler-On-Wheels radar observations made during the Convective and Orographically-induced Precipitation Study (COPS) on 12 August 2007 showed that precipitating clouds only developed between the north–south orientated Murg and Nagold Valleys of the northern Black Forest. The clouds produced moderate precipitation. The Weather Research and Forecasting (WRF) model run at 700 m horizontal resolution in the inner domain was able to simulate the location of the precipitation. Insight is therefore gained into the physical mechanisms responsible for the initiation and development of the convection. Convergence lines resulting from thermally driven flows constrained the initial location of the convection within warm and moist cores produced by heating on elevated surfaces. The heaviest precipitation was later produced by secondary convection, which was initiated within the cores at the boundary between cold-pool outflows and thermal flows.

Key Words: elevated heating; convergence; cold-pools; WRF

Received 19 February 2010; Revised 12 October 2010; Accepted 24 November 2010; Published online in Wiley Online Library 11 February 2011

Citation: Bennett LJ, Blyth AM, Burton RR, Gadian AM, Weckwerth TM, Behrendt A, Di Girolamo P, Dorninger M, Lock S-J, Smith VH, Mobbs SD. 2011. Initiation of convection over the Black Forest mountains during COPS IOP15a. *Q. J. R. Meteorol. Soc.* **137**: 176–189. DOI:10.1002/qj.760

1. Introduction

The forecasting of convective precipitation in hilly terrain is important because of the devastating flooding that can be caused by intense precipitation (e.g. Rotach *et al.*, 2009a, 2009b). Such events can be highly localized and very-high-resolution numerical weather prediction (NWP) models are needed to represent them. The central issue is to determine why precipitating convection breaks out and develops where and when it does (e.g. Aoshima *et al.*, 2008, Weckwerth *et al.*, 2011). The phenomena responsible for triggering convection are well known (Jorgensen and Weckwerth, 2003; Bennett *et al.*, 2006). However, the forecasting skill for heavy convective showers and thunderstorms over orography is still low, mainly because of the poor representation of boundary-layer processes over complex terrain and the interactions of the aerosols, microphysics and dynamics in the convective clouds (e.g. Kottmeier *et al.*, 2008; Behrendt *et al.*, 2011;

Corsmeier *et al.*, 2011; Chaboureau *et al.*, 2011). For example, results from German NWP models run for the Black Forest region produce an overestimation and underestimation of precipitation on the windward and lee sides of the mountains, respectively, and a phase error in the diurnal cycle of precipitation leading to the predicted onset of precipitation occurring several hours too early (Wulfmeyer *et al.*, 2008).

One of the earliest studies of convection over high terrain is that of Braham and Draginis (1960). They made aircraft measurements of temperature and humidity over the Santa Catalina mountains in Arizona and found a 'convective core' over or slightly downwind of the mountains. The core was a dry adiabatic column of warm, moist air. It was generated by the heating of the high-level mountain regions that warmed the air immediately adjacent to the slopes, which set up a valley-breeze circulation (Braham and Draginis, 1960). When there was sufficient moisture available, cumulus clouds formed at the top of the core. Raymond and Wilkening (1980) made similar aircraft measurements, but over the San Mateo mountain range in central New Mexico. They measured the air flow in and around the convective core in addition to temperature and humidity. They observed a cloudless convective core 10–20 km wide and 2–3 km deep, with inflow from all directions at low levels and outflow aloft. There was a net weak upward motion superimposed with strong individual updraughts and downdraughts with a wavelength of 3–4 km. However, Demko and Geerts (2010a) later found in the Cumulus Photogrammetric, In Situ and Doppler Observations (CuPIDO) project held over the Santa Catalina Mountains in Arizona, USA that the circulation and especially its upper-level return flow branch are not immediately apparent, since they are overwhelmed by boundary-layer thermals. Raymond and Wilkening (1982) found that the convergent low-level flow measured in the Magdalena Mountains close to the San Mateo Mountains was only slightly larger in cloudy than in dry conditions.

Demko *et al.* (2009) investigated the development of the boundary layer and cumulus clouds in CuPIDO. They found that the anabatic surface wind usually developed shortly after sunrise and peaked close to solar noon. There was some evidence for a toroidal heat-island circulation, with divergence in the upper boundary layer driven by surface heating over the mountain. Demko and Geerts (2010a) compared 1 km resolution Weather Research and Forecasting (WRF) model results with observations made of the convective boundary layer during the development of shallow orographic cumulus convection in CuPIDO. The model captured the observed surface-temperature distribution, as well as the mountain-scale flow in the convective boundary layer (CBL). The model simulations compared well with the surface observations and soundings. There were differences between the model and observed cloud, which was attributed to differences in low-level moisture, as in many such comparisons. Furthermore, they found that cloud shading and convective downdrafts suppressed the surface convergence. The second part of the study (Demko and Geerts, 2010b) examined the CBL during the development of deep convection. The model compared well with observations, although the development of convection was delayed slightly in the model and the depth of the convection was greater than observed, resulting in a greater amount of precipitation. The small differences were caused by the lack of a mid-level lid and dry layer in the model and an underestimation of local soil moisture.

Banta (1984) used an aircraft to observe the evolution of the boundary layer in a broad, relatively flat basin (South Park) in the Colorado Rocky Mountains. He showed that a region of convergence formed near the surface on the leeward side of the mountains where upslope or upvalley winds blowing from lower areas of the valley met with winds from above the nocturnal inversion blowing down from the ridges. The highest moisture was advected from low areas of the Park into the convergence zone and strong and persistent updraughts were observed in the convergence zone. Thus it was a prime region for the initiation of convection. Banta and Schaaf (1987) found that initiation sites for morning thunderstorms in the mountains clustered into genesis zones, associated with the convergence zones discussed by Banta (1984). The location of the initiation sites and the mechanisms that initiate thunderstorms were dependent on the wind velocity and the orientation and size of the mountain range.

Kossmann *et al.* (1999) focussed on determining where over the mountains the convective clouds were initiated. They showed that convective cells occurred over the same location above a particular valley on different days, an observation consistent with the experience of glider pilots. Kossmann *et al.* (1999) suggested that the cells are caused by thermally induced upslope winds over the steep sidewalls of the valley. Fiedler *et al.* (2000), Kossmann and Fiedler (2000), Kalthoff *et al.* (2000) and Kalthoff *et al.* (2009) confirmed that thermally induced slope and valley winds are common, and often result in convergence zones over the mountain crests. Results of the Vertical Exchange and Orography (VERTIKATOR) project discussed by Barthlott *et al.* (2006), for example, showed that these convergence zones are responsible for triggering deep convection.

Meissner *et al.* (2008) studied the initiation of shallow convection in the mountains of the Black Forest with extensive observations made in a specific case on 1 June 2002 during VERTIKATOR. They compared the observations with the Deutscher Wetterdienst Local Model at 2.8 km and 7 km horizontal resolution. The conditions required for the initiation of convection were found to be restricted to the mountain regions because of increased humidity due to the growth of the CBL in the Rhine Valley and evapotranspiration, elevated heating and the regions of convergence caused by upslope and upvalley winds. The location of the convection simulated with the 2.8 km resolution model compared well with satellite observations of the clouds.

In this article, we extend the work of Meissner *et al.* (2008) by comparing the location and timing of the initiation of convection in the Black Forest Mountains simulated with the WRF model run at 700 m resolution, with observations made with the Doppler-On-Wheels radar. The processes found by the model to be responsible for the initiation are examined and some emphasis is placed on the role of small-scale terrain features. The data were gathered during the Convective and Orographically-induced Precipitation Study (COPS), which took place in southeast France and southwest Germany during June–August 2007. The outline of the article is as follows. Section 2 presents an overview of the experiment and observations of the convective clouds. Results from the simulations of the WRF model are presented in section 3 and a summary is given in section 4.

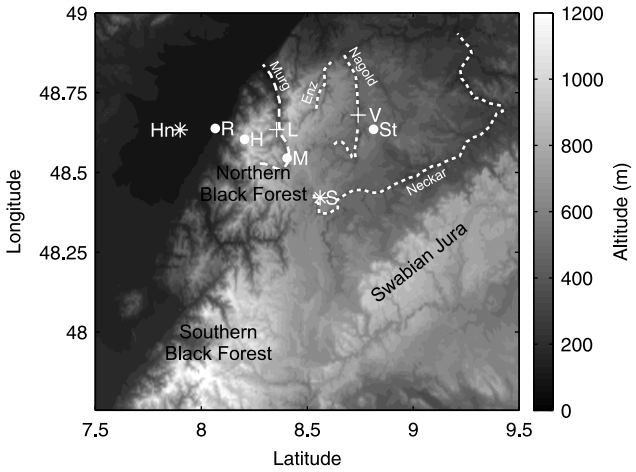

Figure 1. Location of the COPS domain and instrument sites in relation to the topography of the Black Forest mountains: Murg, Enz, Nagold and Neckar rivers (dashed lines), Supersites R: Achern, H: Hornisgrinde, M: Murg and St: Stuttgart (bullets), mobile radar sites Hn: Hohbuhn and S: Schopfloch (asterisks) and automatic weather stations operated by the University of Leeds (L) and the University of Vienna (V) (plus signs).

2. Details of the experiment

2.1. The COPS domain and instrumentation

Detailed descriptions of the COPS scientific and observational strategy can be found in Wulfmeyer *et al.* (2008, 2011). For further technical information on the location and operation of all the COPS instrumentation, the reader is referred to Wulfmeyer *et al.* (2007). A map of the COPS domain and location of the instruments relating to this study is shown in Figure 1.

Two mobile Doppler-On-Wheels (DOW) radars were deployed during IOP15a, at Hohbuhn in the Rhine Valley (DOW2) and Schopfloch in the northern Black Forest (DOW3). The DOW radars are *X*-band (9 GHz) and sensitive to Rayleigh and Mie scattering from insects and precipitation (Wurman *et al.*, 1997). The radars performed a set sequence of plan-position-indicator (PPI) scans (every 0.5° from 0.5°–5°, then 6°, 8° and 10°) from approximately 0730 to 1815 UTC. Radiosondes were launched from Supersites R, H and M throughout the day at approximately three-hourly intervals. A large network of Automatic Weather Stations (AWSs) were operated during COPS and data from two of those stations operated by the University of Leeds and the University of Vienna are used here.

The University of Basilicata Raman Lidar system (BASIL: Di Girolamo *et al.*, 2009) was deployed at Supersite R. It measures temperature and water-vapour mixing ratio based on the application of the rotational (Di Girolamo *et al.*, 2004) and rotovibrational Raman lidar techniques (Whiteman, 2003; Whiteman *et al.*, 2006), respectively, in the ultraviolet region. The data used in this article were integrated over 15 minutes and have a vertical resolution for water vapour and temperature of 150 m and 300 m, respectively, and a precision for water vapour of less than 5% at 2 km and around 20% at 4 km (Bhawar *et al.*, 2011) and for temperature of 1 K up to 4 km. The University of Hohenheim differential absorption lidar (DIAL: Behrendt *et al.*, 2009) and rotational Raman lidar (RRL: Radlach *et al.*, 2008) were deployed at Supersite H.

All times stated within will be given in Universal Coordinated Time, UTC, two hours ahead of Central European Summer Time (CEST). Sunrise on 12 August 2007 was at 0415 UTC (0615 CEST) and solar noon was at 1231 UTC. All heights will be given in metres above sea level (ASL) unless otherwise stated.

2.2. Synoptic conditions

There were no strong synoptic features over the COPS domain on 12 August 2007. A low-pressure system was centred over northwest Scotland, associated with an upper-level trough, whilst a weak upper-level ridge and associated surface high was positioned over central Europe (Figure 2(a)). The slack pressure gradient resulted in light and variable surface flow over the COPS domain. There was diffluent flow at upper levels over eastern France and southwest Germany. Radiosondes launched in the COPS domain at Supersites H and M show stable conditions above the western ridge of the northern Black Forest at 1100 UTC and weak instability ($<200\,\mathrm{J\,kg^{-1}}$ CAPE) slightly downwind of the ridge at 1130 UTC (Figure 2(b) and (c) respectively). Any convection over the ridge generated by surface heating was soon inhibited by a stable region between 850 and 750 mb. The profile was most likely influenced by the advection of air from over the Rhine Valley. However, clouds were able to develop downwind of the ridge as shown by the Murg radiosonde, which observed a well-mixed convective boundary layer (CBL) and saturated conditions between 745 and 640 mb.

2.3. Satellite and radar observations

There was convective precipitation over the Vosges Mountains in southeast France, the Black Forest and the Swabian Jura. Hagen *et al.* (2011), in this issue, investigate the role of the wind profile and low-level convergence for the initiation of convection over the wider COPS domain on 12 and 13 August 2007. This article focuses on the convection observed by the DOW radars over the northern Black Forest.

Satellite images show that there was fog along the Rhine Valley to the west of the Black Forest at 0800 UTC (not shown). Shallow convection developed over the northern and southern Black Forest and Swabian Jura ranges from 0800–1100 UTC (Figure 3(a) and (b), altitude z = 500–1200 m). There was also shallow convection over the lower elevation region (z = 200–400 m) to the northeast of the Black Forest. The convection over the higher terrain deepened between 1100 and 1300 UTC whilst the clouds to the northeast remained shallow (Figure 3(c) and (d)). Heavy precipitation was observed by the network radars associated with deeper convection over the southern Black Forest and Swabian Jura, and lighter precipitation was observed over the northern Black Forest. The location and track of the clouds over the northern Black Forest was examined in more detail using the DOW radars.

Due to the large range and altitude difference between the two DOW radars, dual-Doppler coverage was limited. The convection was also mostly confined to the mountains, therefore only data from DOW3 at Schopfloch (Figure 1) was examined. Using the sequence of PPI scans, every significant echo (> 20 dBZ) measured by DOW3 was manually traced back (forward) in time to its first (last) discernible echo, from any elevation angle. All the echoes were observed between

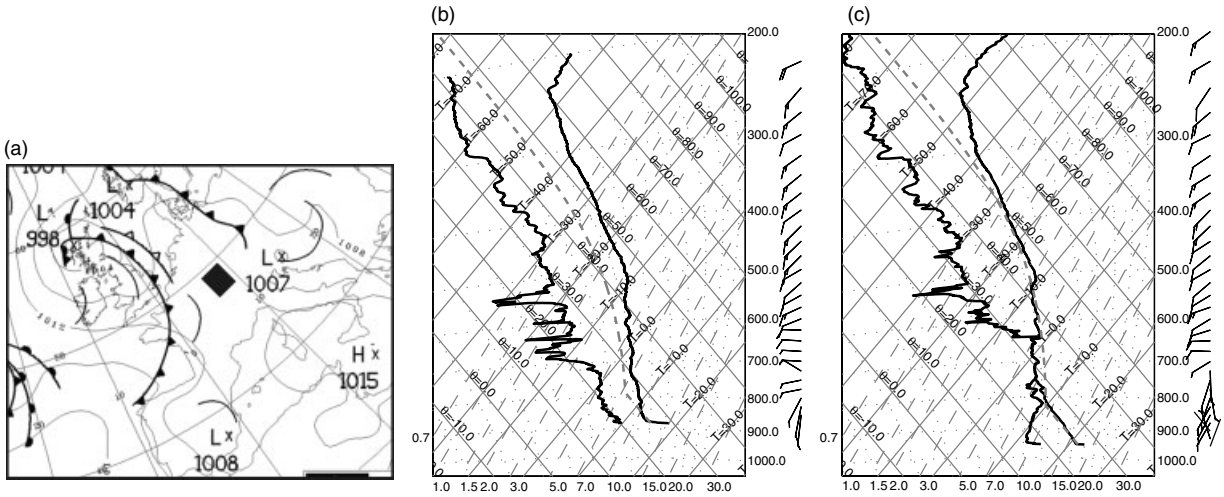

Figure 2. Synoptic conditions over the COPS domain on 12 August 2007: (a) Surface analysis of sea-level pressure and fronts at 1200 UTC on 12 August 2007 (Crown copyright, the Met Office). The black box corresponds to the approximate location of the COPS domain. Also shown are radiosondes launched at (b) Supersite H at 1100 UTC and (c) Supersite M at 1130 UTC. The dashed grey lines represent adiabatic parcel ascents using an average of the lowest 50 mb of the profile to characterize the boundary-layer properties.

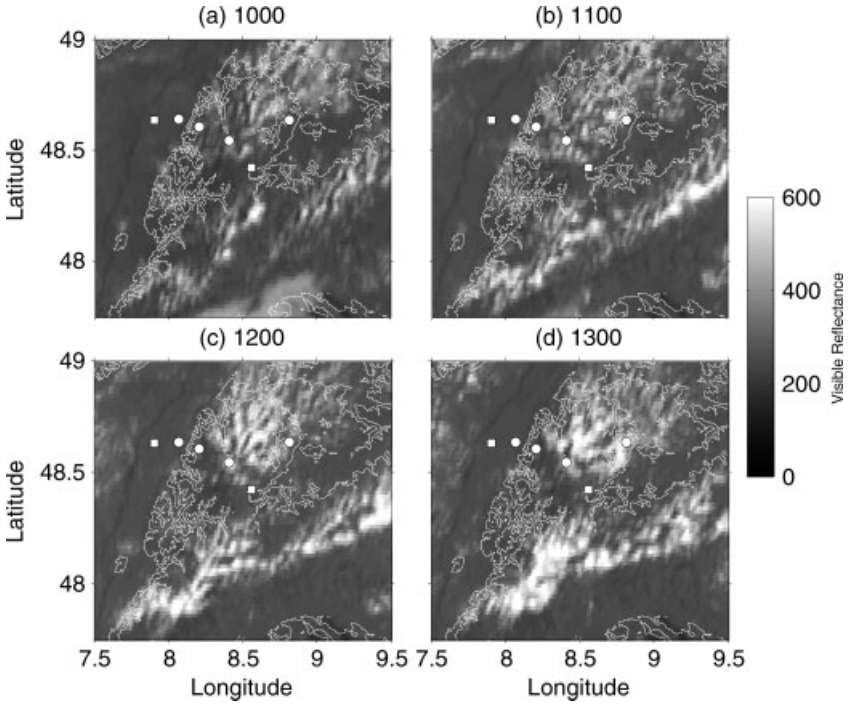

Figure 3. Meteosat second-generation visible reflectance at (a) 1000, (b) 1100, (c) 1200 and (d) 1300 UTC. Supersite locations are marked with circles and DOW radars with squares. The white line contours are terrain heights of 300 m and 500 m.

1100 and 1400 UTC; examples are shown in Figure 4. The initiation and dissipation locations are plotted in Figure 5. The early cumulus clouds were not resolved in enough detail in the satellite images to be able to trace their development back in time prior to the first radar echo. However, advection of the clouds was limited due to a weak westerly steering flow, which was lower than 4 m s^{-1} for z = 2–3 km. The distance between the initiation location determined from satellite and radar is believed to be minimal.

It is clear from Figure 5 that the precipitating clouds all developed in a confined region bounded by the Murg Valley to the west, the Enz Valley to the northwest and the Nagold Valley to the east (Figure 1). The convective cells had maximum reflectivities of 50 dBZ, average lifetimes of 36 min (corresponding to an average distance of less than 10 km) and reached altitudes of 4.5–5 km.

3. Model results

3.1. *Model set-up*

The WRF model Version 3.1 was run for this case using two-way nested domains with 6.3, 2.1 and 0.7 km grid spacing and 121 vertical levels (Figure 6). The inner domain covered the whole of the Black Forest and part of the Rhine Valley. Global Forecast System (GFS) 1° analyses were used to initialize the simulation at 0000 UTC and as lateral boundary conditions on the outer domain at each time step, linearly interpolated between each six-hourly analysis. Although there is a large

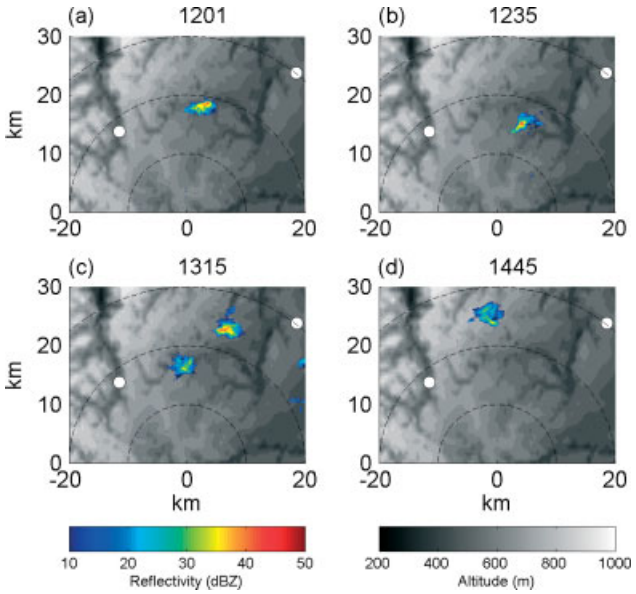

Figure 4. Examples of cells observed by DOW3 between 1100 and 1400 UTC. The greyscale contours are terrain height, the colour contours are reflectivity, the black dashed lines are 10 km range rings and the white circles are the locations of Supersites M and S. The region shown extends from 8.29–8.83° longitude and 48.42–48.69° latitude.

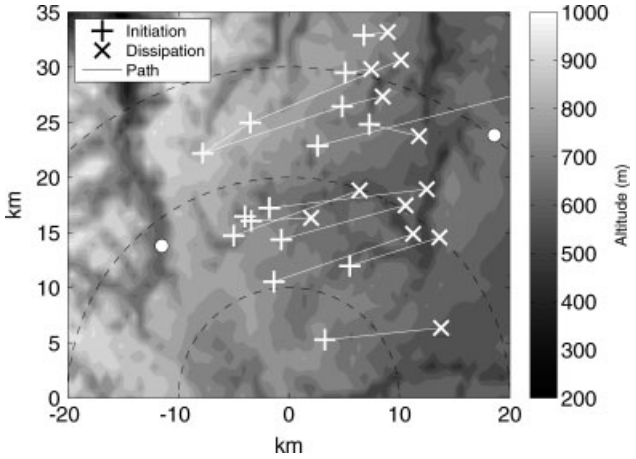

Figure 5. Initiation (plus signs), dissipation (crosses) and path (solid lines) of the echoes observed by DOW3. Background greyscale contours are terrain height and the white circles are the locations of Supersites M and S. The region shown extends from 8.29–8.83° longitude and 48.42–48.74° latitude.

step between the GFS grid and the first model domain, this case is one of weak synoptic forcing and therefore the large-scale conditions are well represented by the initial fields. Model output was produced every 5 min for the inner domain and every 60 min for the middle and outer domains.

The simulations used the following schemes: Morrison double-moment microphysics, Dudhia short-wave radiation and rapid radiative transfer model (RRTM) long-wave radiation, Mellor–Yamada–Janjic (MYJ) planetary boundary layer (a TKE-based scheme) and surface-layer physics, and Noah land-surface model (LSM). The Noah LSM carries soil moisture and temperature at four levels. The Betts–Miller–Janjic cumulus parametrization scheme was applied on the outer domain only. A full description of all these schemes can be found in Skamarock *et al.* (2008).

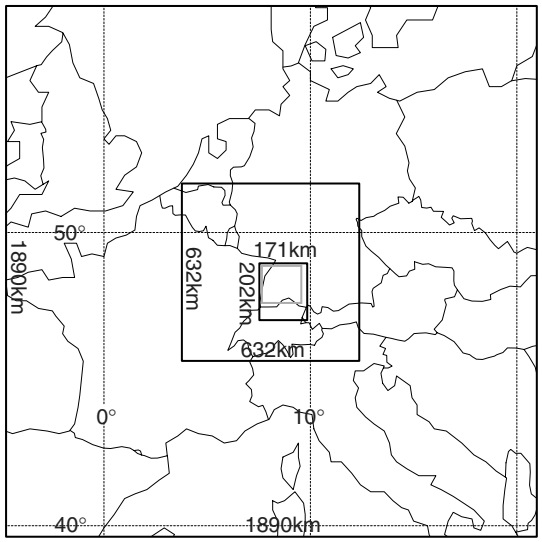

Figure 6. Coverage of the three domains used in the WRF simulations. The grey box in the centre corresponds to the domain shown in Figure 1.

3.2. *Comparison of model results with observations*

The simulated surface wind field, cloud location and precipitation is shown in Figure 7 for a subset of the inner domain at eight different times from 0500–1130 UTC in order to provide an overview of the flow field over the Black Forest and the initial development of the clouds and precipitation. The surface winds are downslope and downvalley at 0500 UTC in the region of the highest peaks and in the Murg, Enz and Nagold Valleys (Figure 7(a)), as expected from cold-air drainage, a commonly observed feature of the diurnal cycle in mountainous terrain (Whiteman, 2000). There is a larger-scale southwesterly flow in the eastern half of the domain. In the southeast, this flow appears to be a drainage flow along the River Neckar Valley.

Whiteman (2000) describes how there is commonly a flow reversal as the valley sides heat up following sunrise, causing air to ascend up the slopes and subsequently up the valleys to replace it. This is evident in the model surface wind field at 0800 (Figure 7(b)). There is flow up the Murg Valley in particular and up the local slopes at the edges of the valley. The flow has only just begun to reverse in the Nagold Valley, perhaps because the slopes are not as steep. The flow is southwesterly along the Rhine Valley, except along the eastern slopes where it is upslope almost everywhere. The southwesterly flow veers to the west and northwest around the northern edge of the Black Forest, particularly at the entrance into the Murg and Nagold Valleys, due to thermal forcing.

Figure 8 shows a comparison of the surface wind field between WRF and three AWSs, located in the Murg and Nagold Valleys (Figure 1). There is an overall good correlation between the model and observed winds. There was a sharp shift in the wind direction observed by the northern AWS in the Murg Valley from southerly to north–northwesterly at about 0845 UTC. The model wind direction switches from a southerly to a north–northeasterly flow, although approximately 1 h 15 min earlier than the observations (Figure 8(a)). The winds at Supersite M, 10 km further south in the Murg Valley, and in the Nagold Valley on the eastern side of the domain were more variable and

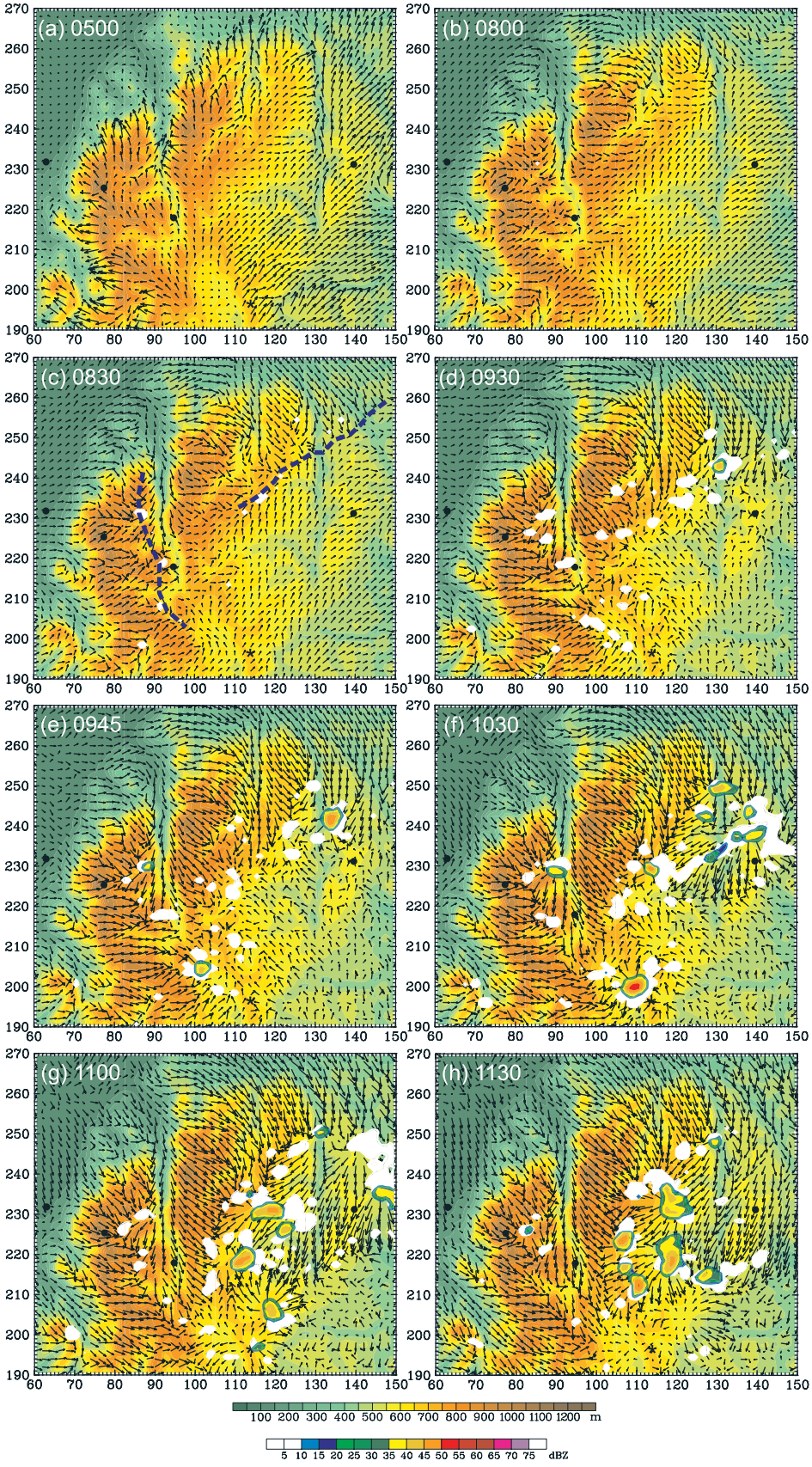

Figure 7. WRF model output for a subset of the inner domain, 48.4–48.9° latitude and 8.1–8.9° longitude, at (a) 0500, (b) 0800, (c) 0830, (d) 0930, (e) 0945, (f) 1030, (g) 1100 and (h) 1130 UTC. Orography is represented by the green–yellow–brown contours. The black vectors are terrain-following winds from the lowest model level, approximately 30 m AGL, and every second vector is plotted. Cloud cover, in white, is plotted at 2.5 km and surface reflectivity is represented by the blue–yellow–red contours. The black bullets correspond to the Supersite locations and the asterisk is the location of DOW3 at Schopfloch (Figure 1). The two dashed blue lines correspond to regions of convergence described in the text.

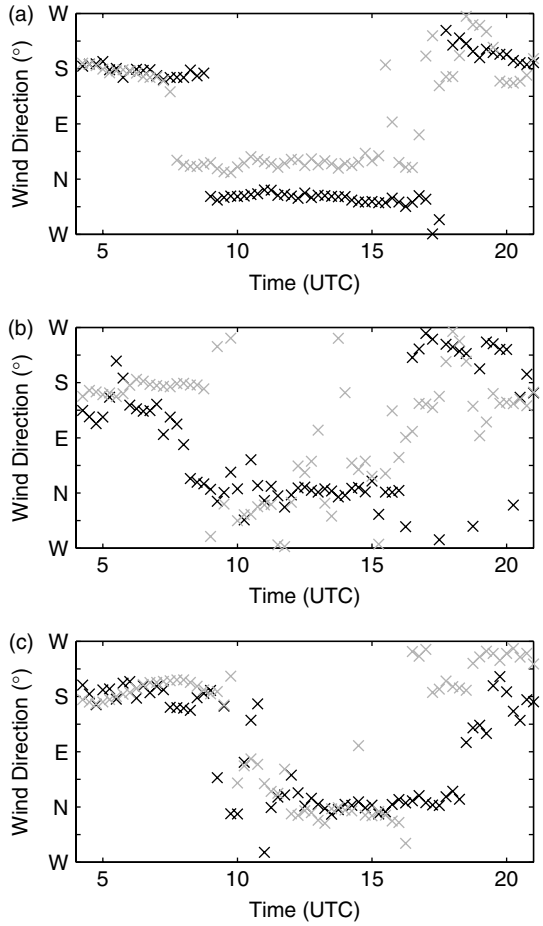

Figure 8. Comparison of wind direction time series between WRF (grey) and three AWSs (black) located (a) in the Murg Valley east of Hornisgrinde ($z = 463$ m), (b) at Supersite M ($z = 511$ m) and (c) on the slopes of the Nagold Valley ($z = 529$ m). The location of the AWSs is shown in Figure 1.

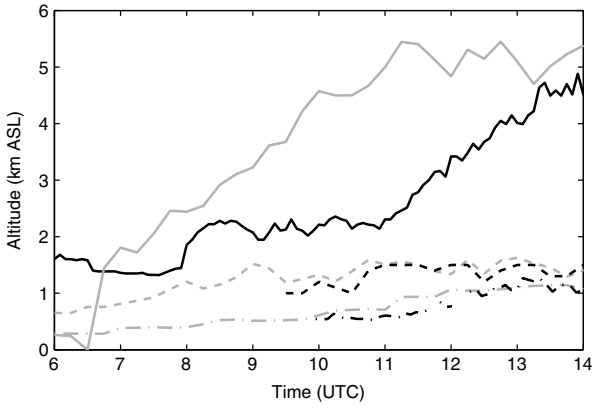

Figure 9. Comparison of observed (black) and modelled (grey) cloud-top height (solid lines) and CBL height at Supersites M (dashed lines) and R (dotted lines).

the switch in direction was not as sharp (Figure 8(b) and (c)). The higher variability could be due to the different shape of the valleys at these locations. The Murg Valley is not as deep or as wide at Supersite M, as it is further north, and the Nagold Valley is a much smaller, shallower valley. The winds also became more variable due to the presence of clouds and precipitation.

Another significant feature is the westerly downslope flow to the lee of Hornisgrinde and the northwesterly downslope flow downwind of the Murg Valley. These downslope flows in the lee of topographic barriers are commonly observed (Jiang *et al.*, 2005). A region of convergence is created where the downslope flow in the lee of Hornisgrinde meets the thermal upslope flow from the Murg Valley (Figure 7(c)), similar to the observations of Banta (1984). To the east of the Murg, the combination of the upvalley flow in the northeast, the westerly downslope flow and the southwesterly flow over the Neckar and Nagold Valleys leads to a second zone of convergence, orientated northeast–southwest (Figure 7(c)). Model clouds form and develop along both of these convergence zones (Figure 7(d)).

The first precipitation develops in a cloud over the Nagold Valley (Figure 7(d)). Soon afterwards, precipitation has also developed in the clouds on the lee side of Hornisgrinde (Figure 7(e)). However, the observed clouds in this location did not precipitate. The model clouds over the Nagold Valley are larger and produce more precipitation than those to the west. Cold-pool outflows from this precipitation propagate towards the southwest, causing convergence with the downslope northwesterly flow and generating secondary convection (Figure 7(f)–(h)). It is evident from Figures 5 and 7 that the location of the dominant precipitating convection simulated by the model compares very well with the observations.

The visible satellite and radar observations showed that there was widespread shallow convection over the Black Forest between 0800 and 1100 UTC, followed by deeper precipitating convection from 1100–1400 UTC (see section 2). This is also confirmed by the time series of cloud-top height (CTH) derived from 5-min infrared satellite data (Figure 9). CTH was derived by extracting the minimum brightness temperature in the region bounded by 8.2–8.8° longitude and 48.5–48.8° latitude and comparing it with the temperature profile from radiosondes launched at Supersite H. The shallow cumulus clouds were first identifiable in the MSG visible channel data from about 0730 UTC and had maximum tops of 2.3 km between 0800 and 1100 UTC, initially capped by a stable layer at 750 mb (Figure 2(b)). The clouds then grew at a rate of 0.24 m s^{-1} between 1100 and 1400 UTC up to a maximum altitude of 4.9 km, where they were capped by a stable layer at about 500 mb (Figure 2(b) and (c)).

CTH is a diagnosed variable in the model output and the maximum CTH was extracted for the same region as for the observations. Figure 9 shows that model clouds developed about 70 min earlier than the observed clouds and that the model did not reproduce a period of shallow convection before deeper convection developed. Despite a similar region of stability in the model profile at 750 mb (not shown), clouds were not capped and developed to a maximum altitude of 5.4 km by 1115 UTC. However, the growth rate of model clouds (between 0645 and 1115 UTC) was also 0.24 m s^{-1}, agreeing remarkably well with the observations. There is also a good comparison of CBL depth between the model and observations (Figure 9); the average difference was approximately 120 m. The largest differences at Supersite M occurred between 0930 and 1100 UTC, when the observed convection was capped at 2.3 km but the model clouds were deepening. As will be discussed below, the model overestimated humidity in the CBL, which produced enough instability for clouds to develop past the lid. Although model clouds reached slightly higher altitudes than the observed ones,

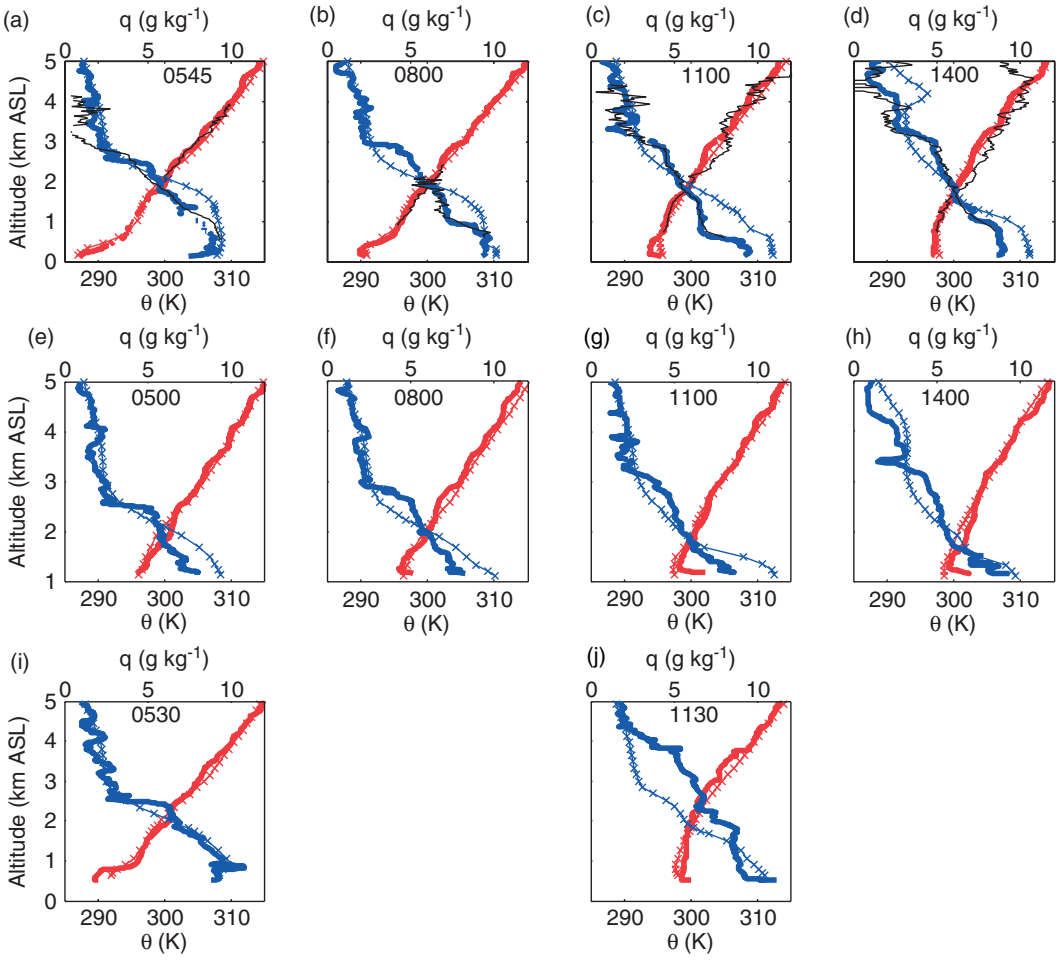

Figure 10. Vertical profiles of potential temperature and mixing ratio from the WRF model and observations, for (a)–(d) Achern, (e)–(h) Hornisgrinde and (i)–(j) Murg Supersites. Key: WRF data are shown by lines with crosses, radiosondes by solid lines and the Raman lidar BASIL by black lines in (a)–(d).

they were also ultimately capped by the stable layer at 500 mb.

3.3. *Comparison of observed and model profiles*

A comparison between observed and simulated vertical profiles of potential temperature (θ) and mixing ratio (q) is shown in Figure 10 for Supersites R, H and M. The observed CBL at Achern developed to a depth of $z = 540$ m at 1100 UTC and $z = 1$ km at 1400 UTC (Figure 10(c) and (d)). The difference between the observed and simulated CBL depth is less than 150 m and the difference in the magnitude of θ within this layer is less than 0.5 K. Above the CBL, the difference in θ is typically 1.5 K. The difference between the average value of q in the CBL is about 1.7 g kg^{-1} at both 1100 and 1400 UTC, with the model being moister than the observations. Above the CBL and up to about 2 km the average simulated and observed q differ by 2–3 g kg^{-1}.

The observed profiles of θ and q at Hornisgrinde were not as well mixed as at Achern and it is therefore more difficult to deduce the top of any CBL (Figure 10(e)–(h)). There is an indication of a superadiabatic surface layer and a very shallow CBL at 0800 UTC. The simulated values of θ and q within the CBL are about 0.8 K and 1.5 g kg^{-1} greater, respectively, than the observations at this time. By 1100 UTC, the observed and simulated CBL depth has increased only marginally to about 300 m AGL. The simulated average value of θ within the CBL was about 1 K less than the observed value and the value of q was 1.5–2 g kg^{-1} greater than observed. It has been noted before that the use of the MYJ boundary layer scheme tends to result in a cooler, moister boundary layer (Weisman *et al.*, 2008).

Measurements with the University of Hohenheim DIAL and RRL confirmed that the CBL was shallow above Hornisgrinde during the whole day (CBL top height, $z < 500$ m AGL, not shown). During the period 0830–1430 UTC, broken shallow clouds were frequent, with bases from close to the ground to 450 m AGL. These clouds were a combination of forced lifting and locally driven turbulent mixing during periods of limited solar insolation. The atmosphere became free of clouds above Hornisgrinde between 1430 and 1600 UTC. Nevertheless, the CBL stayed shallow ($z < 500$ m AGL).

There is a good comparison between the 0530 UTC radiosonde launched at Supersite M and the model profile (Figure 10i). However, there are large differences between the mixing-ratio profiles of the model and observations at 1130 UTC (Figure 10j). The model is several g kg^{-1} drier than the observations for $z = 1.5$–4.5 km. This is likely to be due in part to the ascent of the radiosonde through a cloud for $z = 2.6$–3.8 km, as revealed by 100% relative humidity at these altitudes (not shown).

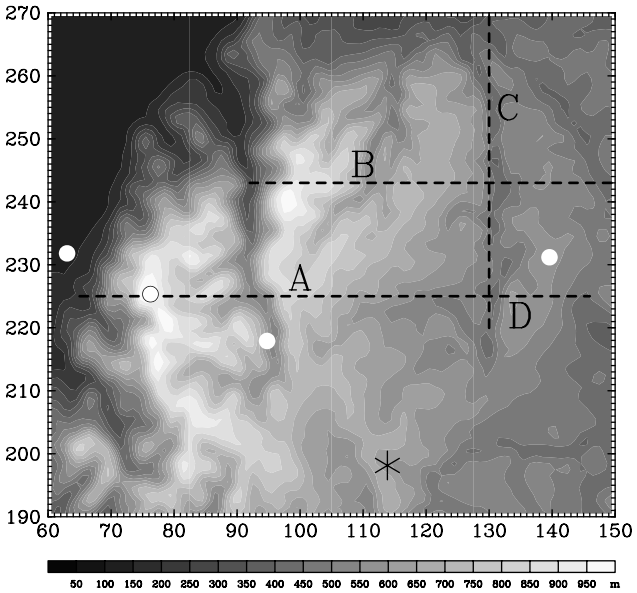

Figure 11. Location of cross-sections in relation to the orography and Supersites. The axis numbers refer to grid points in the inner domain, where the spacing is 700 m. The cross-section locations in the order in which they are discussed are A: $x = 65$–125 and $y = 225$, B: $x = 92$–150 and $y = 243$, C: $x = 130$ and $y = 220$–270 and D: $x = 74$–146 and $y = 225$. Supersites are marked with bullets and DOW3 with an asterisk.

3.4. *Processes leading to the initiation of convection*

The physical effects that were responsible in the model for the formation and development of convection over the Black Forest region were heating on elevated surfaces (hereafter called elevated heating) that formed warm and moist cores, convergence lines produced by thermal flows that controlled the location of the strongest convection within the cores, and outflows from convective clouds that produced further convergence lines. We illustrate how the convection develops as a result of these processes in this section, using a series of vertical cross-sections of virtual potential temperature (θ_v) and wind. The reader is referred to Figure 11 for the location of the four cross-sections discussed below.

The CBL is very shallow over the mountains in the morning in both the model results and observations (Figures 10(f) and (g) and 12(a)), probably because of the advection of the cold, stable air mass from over the Rhine Valley. Low clouds were also observed, which would have reduced solar insolation, however these were not simulated by the model. The wind is lower than 2 m s^{-1} below $z = 1.5$ km, but gradually increases to about 5 m s^{-1} by $z = 5$ km. There is air flow (less than 0.3 m s^{-1}) up the western side of Hornisgrinde, which close inspection revealed was due to heating on the valley slopes, as described in section 3.2. The air flow has a downward component on the lee side of Hornisgrinde, which brings slightly higher θ_v air downwards and causes the contours to be parallel to the slope. There is also an increase in θ_v near the surface, indicating positive surface fluxes of heat and moisture. The combination of downward motion due to the downslope flow and the surface fluxes results in a higher θ_v region from the surface to $z = 1.2$ km.

Figure 12(b) shows that a vertical column of higher θ_v air has formed by 0740 UTC centred on $x = 14$ km, and there is an updraught associated with it. Individual cross-sections of potential temperature and mixing ratio reveal that this

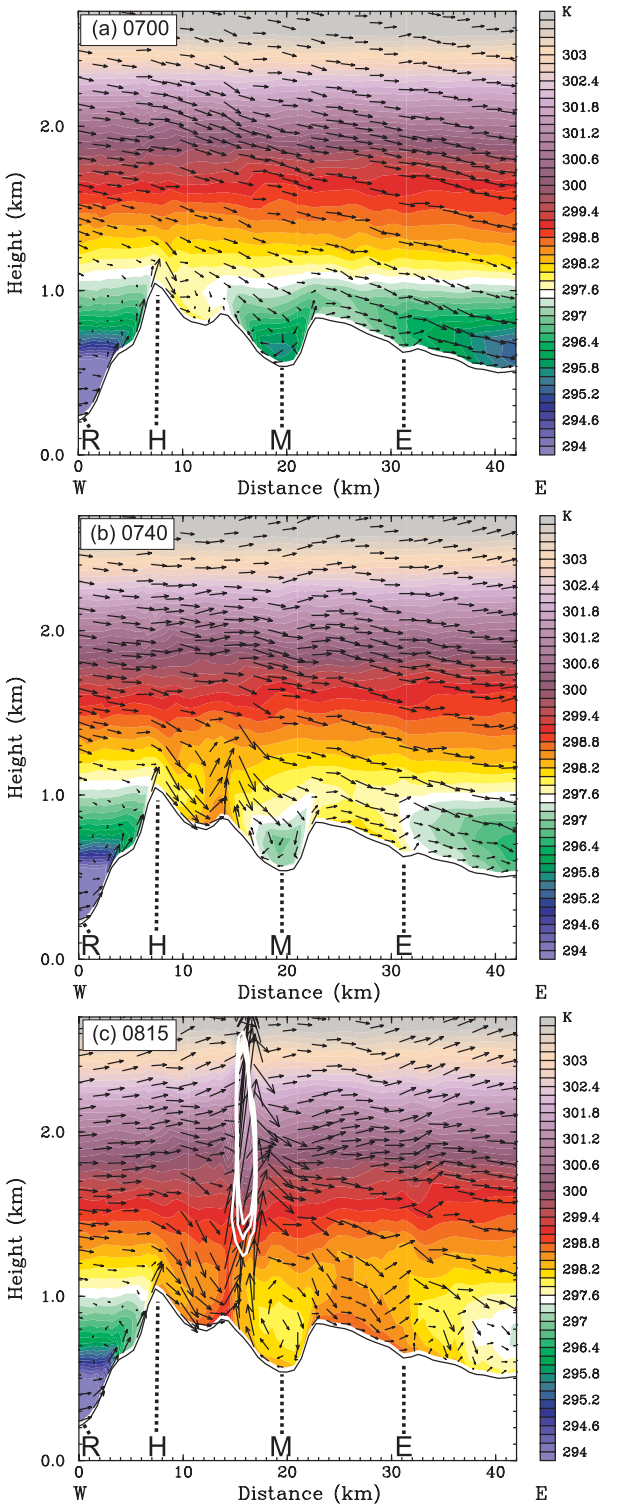

Figure 12. Cross-section A (Figure 11) of θ_v (colour contours) and wind vectors in the x–z plane at (a) 0700, (b) 0740 and (c) 0815 UTC. The white contours are cloud water mixing ratio at 0.05, 0.2 and 0.8 g kg^{-1}. The maximum horizontal and vertical vectors are (a) 2.8 and 0.3 m s^{-1}, (b) 3.0 and 0.3 m s^{-1} and (c) 3.5 and 1.2 m s^{-1}. Every second vector is shown. Hornisgrinde and the Rhine, Murg and Enz Valleys are labelled H, R, M and E, respectively.

region is both warm and moist. This column of higher θ_v is similar to the core of warmer air that has been observed to form over mountains by Raymond and Wilkening (1980), for example, as a result of an elevated heat island.

There are two additional features to notice in Figure 12(b). Firstly, the downward flow on the lee side of Hornisgrinde

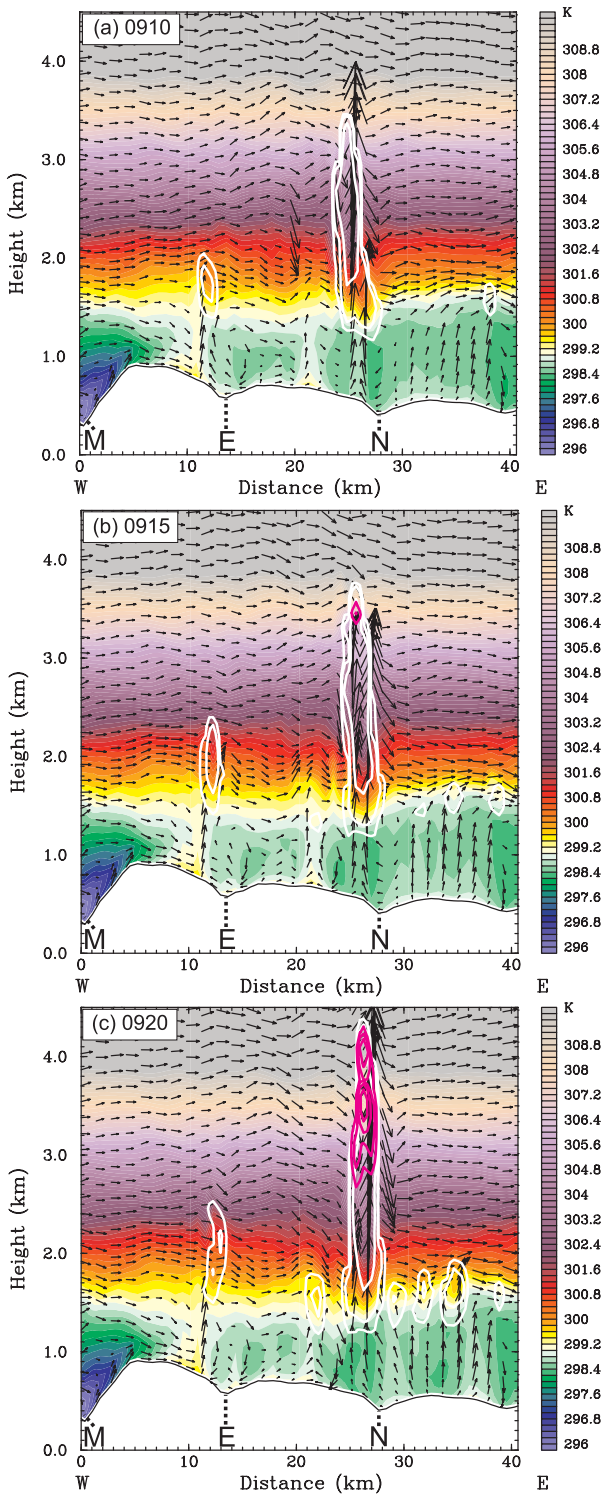

Figure 13. Cross-section B (Figure 11) of θ_v (colour contours) and wind vectors in the x–z plane at (a) 0910, (b) 0915 and (c) 0920 UTC. White contours are cloud water mixing ratio at 0.05, 0.2 and 0.8 g kg^{-1} and the pink contours are total precipitation mixing ratio at 0.05, 0.1, 0.2 and 0.4 g kg^{-1}. The maximum horizontal and vertical vectors are (a) 4.2 and 4.4 m s^{-1}, (b) 4.0 and 3.5 m s^{-1} and (c) 4.2 and 4.6 m s^{-1}. Every second vector is shown. The Murg, Enz and Nagold Valleys are labelled M, E and N, respectively.

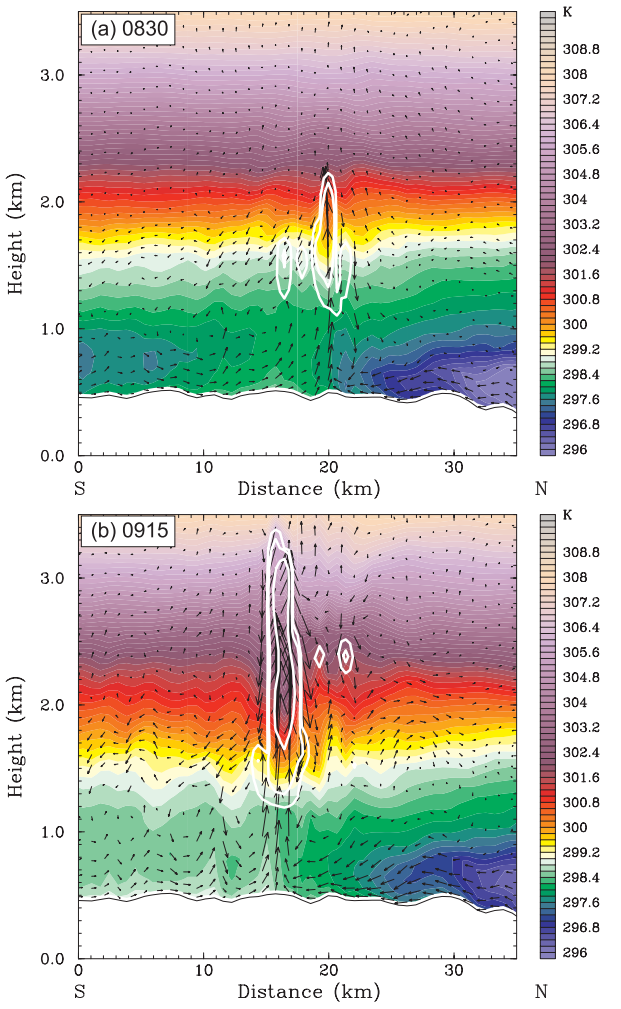

Figure 14. Cross-section C (Figure 11) of θ_v (colour contours) and wind vectors in the y–z plane at (a) 0830 and (b) 0915 UTC. The maximum horizontal and vertical vectors are (a) 2.8 and 1.1 m s^{-1} and (b) 4.1 and 3.1 m s^{-1}. Every second vector is shown. Contours of cloud water mixing ratio are shown in white at 0.05, 0.2 and 0.8 g kg^{-1}.

is more prominent between the surface and $z \sim 1.4$ km than at 0700 UTC. However, the time sequence of model cross-sections shows that upward motion does not occur until there is surface heating. Secondly, the upslope flow on the west side of the Murg Valley (x = 15–18 km) is stronger than at 0700 UTC as a result of heating of the valley sides. A region of convergence has formed at x = 15 km, over the ridge on the west side of the valley, and eventually a shallow cloud develops above it at 0755 UTC with a base at z = 1.3 km, about 400 m above the ground, although only 250 m above Hornisgrinde.

The value of θ_v continued to increase in the column over the ridge and a 1.4 km deep cloud has formed slightly downwind of the ridge by 0815 UTC (Figure 12(c)). Values of θ_v have also increased along the slope downwind of the Murg Valley, creating another warm, moist core centred on x = 26 km and extending to z = 1.2 km. However, there are no clouds over this region at this time. The clouds on the west side of the Murg Valley experience several pulses of growth and decay between 0815 and 1000 UTC, reaching maximum depths of 2.3 km (and cloud tops of 3.5 km). No precipitation was produced in these particular clouds; however, precipitation did occur in another cloud situated 3.5 km to the north of this location, starting at about 0935 UTC, and reached the ground at 0945 UTC (Figure 7(e)).

The first precipitation to occur east of the Murg Valley was produced in a cloud that formed on the convergence line near the Nagold Valley (Figure 7(c) and (d)). Figure 13(a)–(c)

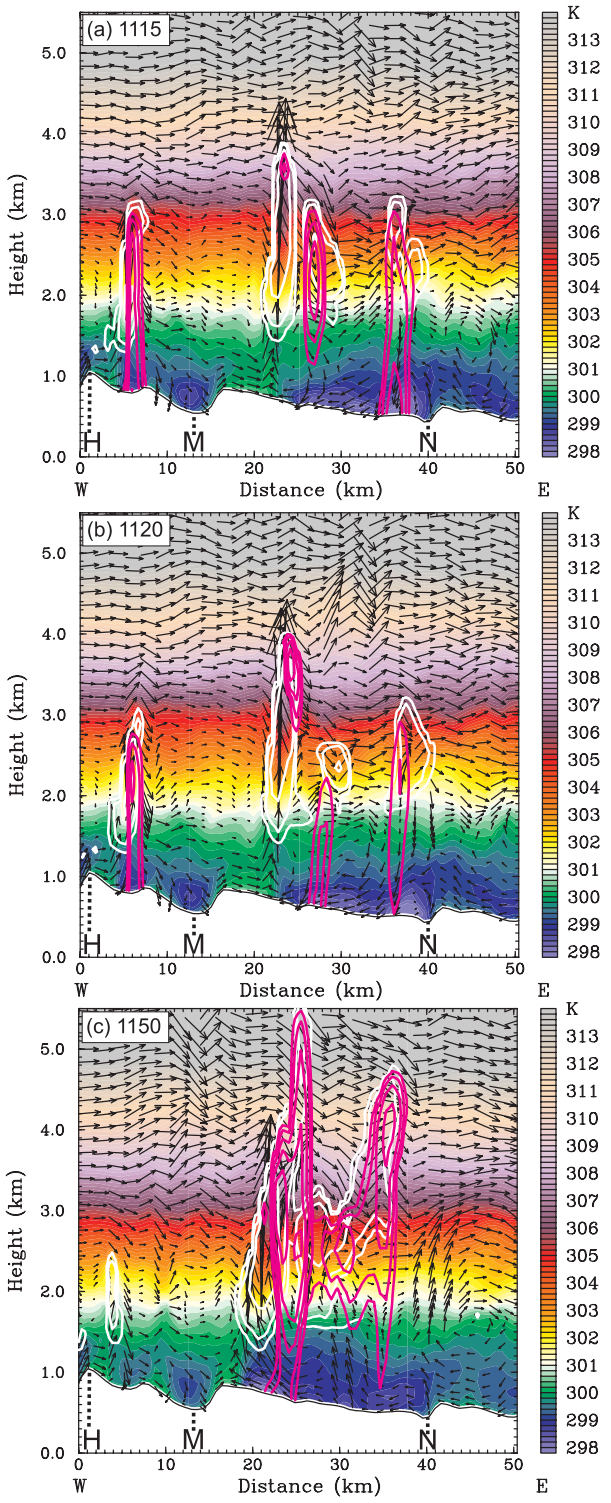

Figure 15. Cross-section D (Figure 11) of θ_v (colour contours) and wind vectors in the x–z plane at (a) 1115, (b) 1120 and (c) 1150 UTC. Contours of cloud water mixing ratio at 0.05, 0.2 and 0.8 g kg^{-1} are shown in white and total precipitation mixing ratio at 0.05, 0.1, 0.2, 0.4 and 0.8 g kg^{-1} are in pink. Maximum horizontal and vertical vectors are (a) 3.2 and 1.9 m s^{-1}, (b) 6.7 and 4.3 m s^{-1} and (c) 8.0 and 4.2 m s^{-1}. Every second vector is shown. Hornisgrinde and the Murg and Nagold Valleys are labelled H, M and N, respectively.

shows a sequence of cross-sections through this cloud at 0910, 0915 and 0920 UTC as the precipitation is developing. The cloud develops on the west side of the Nagold Valley where there is convergence between the northerly and southwesterly flows discussed in section 3.2, but also due to flow up the sides of the valley. The main convergence is in the north–south plane, perpendicular to the cross-section. Cloud base is about 1.2 km and cloud top at 3.4 km at 0910 UTC, but there is no precipitation. It is interesting that the values of θ_v near the surface are greatest above the highest elevations and least above the lowest. Another warm, moist core has also developed on the ridge between the Murg and Enz Valleys. There is convergence at its eastern edge between the downslope westerly flow and easterly flow up the side of the Enz Valley. There are also a number of updraughts in the boundary layer between $x = 30$–40 km and small clouds form within them by 0920 UTC (Figure 13(c)). Precipitation has just formed in the largest cloud at 0915 UTC at $z = 3.4$ km (Figure 13(b)) and is well-developed 5 min later at 0920 UTC (Figure 13(c)). It continues to develop and reaches the ground at 0930 UTC over the Nagold Valley (Figure 7(d)).

Since the convergence line plays such an important role in the formation and development of the first precipitating convection, we show a north–south cross-section along the Nagold Valley in Figure 14. The low-level convergence can be seen at 0830 UTC in Figure 14(a), corresponding with Figure 7(c). There is a southerly flow down the Nagold Valley that meets the relatively cooler northerly flow up from the entrance of the valley. There is an updraught of just less than 2 m s^{-1} and a shallow cloud has formed. However, this cloud and other similar ones that form on the convergence line do not develop further until about 0915 UTC (Figure 14(b)), by which time there has been an increase in θ_v in the lowest levels. This indicates that the uplift due to the convergence line caused by anabatic flows is not sufficient for the development of precipitating convection.

As seen in Figure 7(f)–(h), the early precipitation in the northeast of the domain over the Nagold Valley produced outflows that interacted with the northwesterly downslope flow east of the Murg Valley to produce new regions of convergence and secondary precipitating convection. A cross-section through a cloud that formed by this process is shown in Figure 15(a)–(c). The cloud is located at $x = 22$ km at 1115 UTC (Figure 15(a)) on the eastern edge of a warm, moist core that extends from $x = 16$–23 km. The convergence between the downslope flow and the cooler outflow moving upslope is very clear and produces a significant updraught. A cloud has formed as a result of the updraught and precipitation has just started to form via the warm rain process at $z = 3.7$ km. The precipitation has developed further by 1120 UTC (Figure 15(b)), mainly on the downshear side of the cloud. By 1130 UTC the precipitation has reached the ground (Figure 7(h)) and appears to reinforce the original outflow. The outflow continues to move upslope, forcing convergence with the remaining warm, moist core and westerly flow and new updrafts are generated. The cloud has ascended to $z = 5.5$ km by 1150 UTC ($T \sim -12$°C; Figure 15(c)) and the cold-air outflow near the surface has almost reached the top of the slope. No clouds grew to heights greater than about 5.5 km in the model, due to warmer air aloft capping the convection.

In the model simulations, the outflows from the convection combined together to form a broader-scale northeasterly flow. Although the DOW radar did not observe any signatures of outflow boundaries, i.e. reflectivity fine lines and corresponding wind shifts, it is significant that the radial velocity field did show a corresponding northeasterly flow increasing in strength during the afternoon.

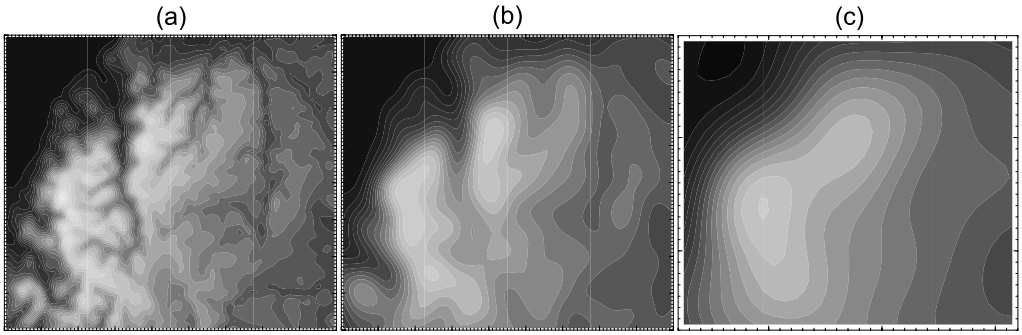

Figure 16. Comparison of orography for the three model simulations: (a) control run, R1, inner domain with 0.7 km grid resolution and 30 arcsec orography, (b) R2 inner domain with 0.7 km grid resolution and 2 arcmin orography and (c) R3 inner domain with 2.1 km grid resolution and 2 arcmin orography.

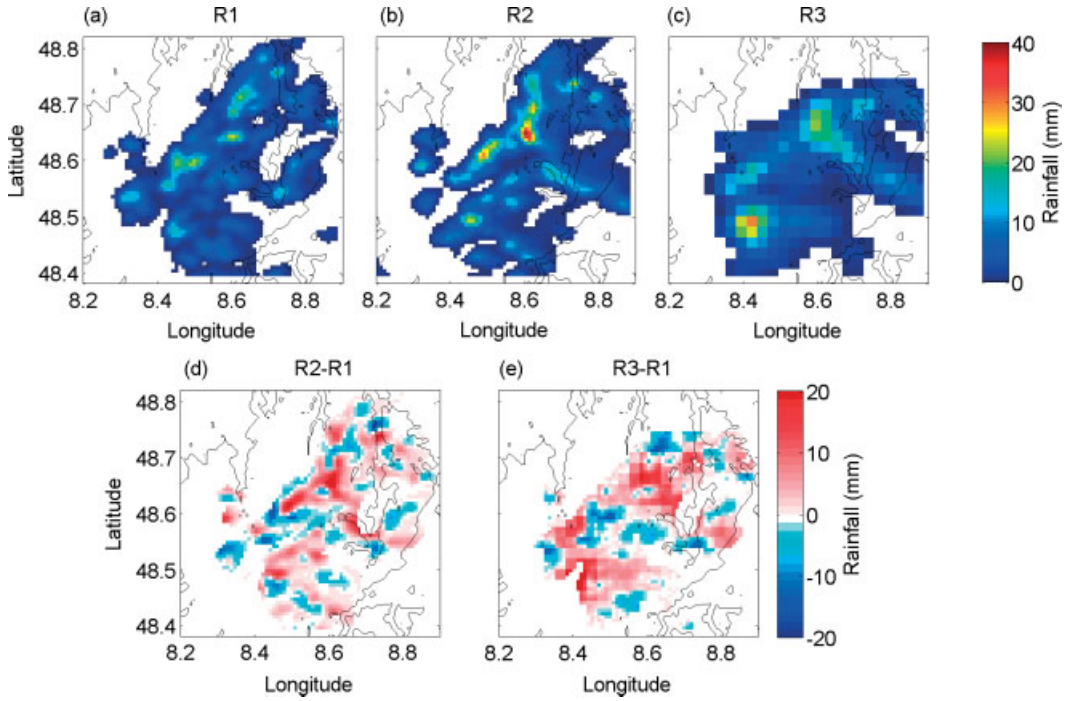

Figure 17. Accumulated rain over the period 0000–1500 UTC for simulations (a) R1, (b) R2 and (c) R3. The differences between R1 and the other two simulations are highlighted in (d) and (e). Data from R3 were interpolated on to the same grid as R1 in order to calculate the differences between the simulations.

3.5. Influence of small-scale terrain features on the initiation of convection

In order to investigate the importance of the small-scale river valleys for the initiation of convection in the northern Black Forest, two additional model runs were performed: (a) the resolution of the orography was reduced (R2) and (b) the model resolution was reduced (R3). More specifically, R2 consisted of the same set-up as the control run (R1), but the resolution of the orography on the inner domain was reduced to that of the middle domain, i.e. from 30 arcsec to 2 arcmin data. For R3 the inner domain was removed, resulting in a two-domain simulation at 6.3 km for the outer domain and 2.1 km for the inner domain. All other parameters remained the same. The orography of the northern Black Forest is shown in Figure 16 for each of the three simulations.

The accumulated precipitation over a 15 h period from 0000–1500 UTC for simulations R1, R2 and R3 is shown in Figure 17(a)–(c). It is clear that R2 causes more intense precipitation in a few localized regions. Rainfall also occurs over a slightly larger area in R2 (36.9%) and R3 (37.4%) compared with R1 (34.5%). The rainfall amounts in R2 are greater and less than the amounts in R1 and R3 by as much as −17 and 26 mm, respectively. On average, over the domain shown, the rainfall amount in R3 is greater than that in R1 by 1.8 mm and twice as much as R2.

The flow is more uniform and stronger down the Murg Valley in R2, for example, hence causing stronger convergence at the head of the valley and stronger convection (not shown). The fine-scale motions are also absent and the convection is larger and more intense. Simulation R3 (2.1 km resolution, Figure 17(c)) produces fewer and larger convective systems with more precipitation. Elsewhere, the smaller-scale features evident in the standard run due to the peaks and valleys are missing.

4. Summary and conclusions

Mobile Doppler radar observations on 12 August 2007 showed that precipitating clouds only developed between the north–south orientated Murg and Nagold Valleys of

the northern Black Forest. The WRF model was used as a tool to investigate the processes responsible for initiating the convection. The model was run with 700 m horizontal resolution in the inner domain of a two-way nested simulation. The higher resolution was needed to capture the fine-scale motions over the complex terrain in order to produce convection in the correct location and of about the right intensity to match observations. The physical effects that were responsible in the model for the formation and development of the convection over the Black Forest region were as follows: elevated heating that formed warm, moist cores; convergence lines produced by thermal flows that controlled the location of the convection within the cores; cold-pool outflows that generated secondary convection where they interacted with the thermal flows.

The convergence lines were generated by the interaction of three air flows: the thermal upvalley and upslope flows, a downslope westerly/northwesterly flow and a southwesterly drainage flow. It is evident from the model results that convection would not form without elevated heating. Warm and moist cores were produced above most of the mountain regions. However, although small clouds formed in several locations within the cores, the strongest clouds were constrained to the regions of convergence produced first by thermal flows and then by outflows from previous convection.

Acknowledgements

We wish to thank the many people involved in COPS, particularly Professor Volker Wulfmeyer and Dr Christian Barthlott. This work was supported by the NERC consortium grant NE/E018483/1. Acknowledgement is made to Computational Modelling Services (CMS) for support of the WRF model runs performed on HECTOR. Manfred Dorninger wishes to acknowledge the Austrian Science Foundation, FWF (grant: 19658-N10) for the contribution of the University of Vienna AWS. We would like to thank Drs Morris Weisman and Stan Trier (NCAR) for very helpful discussions on the modelling, Dr Jay Miller (NCAR) and Tracy Emerson for their help processing DOW data and Dr Martin Hagen (DLR) for his expert advice on radar analysis and helpful comments on the paper. We are very grateful for all those involved in setting up the Leeds AWS network, in particular Dr Barbara Brooks, Matt Hobby and James Groves.

References

Aoshima F, Behrendt A, Bauer H-S, Wulfmeyer V. 2008. Statistics of convection initiation by use of Meteosat rapid scan data during the Convection and Orographically-induced Precipitation Study (COPS). *Meteorol. Z.* **17**: 921–930.

Banta RM. 1984. Daytime boundary-layer evolution over mountainous terrain. Part I: Observations of the dry circulations. *Mon. Weather Rev.* **112**: 340–356.

Banta RM, Schaaf CB. 1987. Thunderstorm genesis zones in the Colorado Rocky Mountains as determined by traceback of geosynchronous satellite images. *Mon. Weather Rev.* **115**: 463–476.

Barthlott C, Corsmeier U, Meissner C, Braun F, Kottmeier C. 2006. The influence of mesoscale circulation systems on triggering convective cells over complex terrain. *Atmos. Res.* **81**: 150–175.

Behrendt A, Wulfmeyer V, Riede A, Wagner G, Pal S, Bauer H, Radlach M, Späth F. 2009. Three-dimensional observations of atmospheric humidity with a scanning differential absorption lidar. *Proc. SPIE* **7475**: 7475L, DOI:10.1117/12.835 143.

Behrendt A, Pal S, Aoshima F, Bender M, Blyth A, Corsmeier U, Cuesta J, Dick G, Dorninger M, Flamant C, Di Girolamo P, Gorgas T, Huang Y, Kalthoff N, Khodayar S, Mannstein H, Träumner K, Wieser A, Wulfmeyer V. 2011. Observation of convection initiation processes with a suite of state-of-the-art research instruments during COPS IOP 8b. *Q. J. R. Meteorol. Soc.* **137**(S1): 81–100, DOI: 10.1002/qj.758.

Bennett LJ, Browning KA, Blyth AM, Parker DJ, Clark PA. 2006. A review of the initiation of precipitating convection in the United Kingdom. *Q. J. R. Meteorol. Soc.* **132**: 1001–1020.

Bhawar R, Di Girolamo P, Summa D, Flamant C, Althausen D, Behrendt A, Kiemle C, Bosser P, Cacciani M, Champollion C, Di Iorio T, Engelmann R, Herold C, Pal S, Riede A, Wirth M, Wulfmeyer V. 2011. The water vapour intercomparison effort in the framework of the Convective and Orographically-induced Precipitation Study: airborne-to-ground-based and airborne-to-airborne Lidar systems. *Q. J. R. Meteorol. Soc.* **137**(S1): 325–347.

Braham RR, Draginis M. 1960. Roots of orographic cumuli. *J. Meteorol.* **17**: 214–226.

Corsmeier U, Kalthoff N, Barthlott C, Behrendt A, Di Girolamo P, Dorninger M, Handwerker J, Kottmeier C, Mahlke H, Mobbs SD, Norton EG, Wickert J, Wulfmeyer V. 2011. Processes driving deep convection over complex terrain: a multi-scale analysis of observations from COPS IOP 9c. *Q. J. R. Meteorol. Soc.* **137**(S1): 137–155, DOI: 10.1002/qj.754.

Chaboureau J-P, Richard E, Pinty J-P, Flamant C, Di Girolamo P, Kiemle C, Behrendt A, Chepfer H, Chiriaco M, Wulfmeyer V. 2011. Long-range transport of Saharan dust and its radiative impact on precipitation forecast over western Europe. *Q. J. R. Meteorol. Soc.* **137**(S1): 236–251.

Demko JC, Geerts B. 2010a.. A numerical study of the evolving convective boundary layer and orographic circulation around the Santa Catalina mountains in Arizona. Part I: Circulation without deep convection. *Mon. Weather Rev.* **138**: 1902–1922.

Demko JC, Geerts B. 2010b.. A numerical study of the evolving convective boundary layer and orographic circulation around the Santa Catalina mountains in Arizona. Part II: Interaction with deep convection. *Mon. Weather Rev.* **138**: 3603–3622.

Demko JC, Geerts B, Miao Q. 2009. Boundary layer energy transport and cumulus development over a heated mountain: an observational study. *Mon. Weather Rev.* **137**: 447–468.

Di Girolamo P, Marchese R, Whiteman DN, Demoz BB. 2004. Rotational Raman Lidar measurements of atmospheric temperature in the UV. *Geophys. Res. Lett.* **31**(1): L01106.

Di Girolamo P, Summa D, Ferretti R. 2009. Rotational Raman Lidar measurements for the characterization of stratosphere–troposphere exchange mechanisms. *J. Atmos. Oceanic Technol.* **26**: 1742–1762.

Fiedler F, Bischoff-Gauß I, Kalthoff N, Adrian G. 2000. Modeling of transport and dispersion of SF6 in the Freiburg–Schauinsland area. *J. Geophys. Res.* **105**(D1): 1599–1610.

Hagen M, van Baelen J, Richard E. 2011. Influence of the wind profile on the location of hotspots of convection in mountainous terrain. *Q. J. R. Meteorol. Soc.* **137**(S1): 224–235, DOI: 10.1002/qj.784.

Jiang Q, Doyle JD, Smith RB. 2005. Blocking, descent and gravity waves: observations and modelling of a MAP northerly föhn event. *Q. J. R. Meteorol. Soc.* **131**: 675–701.

Jorgensen DP, Weckwerth TM. 2003. 'Forcing and organisation of convective systems'. In *Radar and Atmospheric Science: A collection of essays in Honor of David Atlas.*, Wakimoto RM, Srivastava R (eds). American Meteorological Society: Boston; pp 75–103.

Kalthoff N, Horlacher V, Corsmeier U, Volz-Thomas A, Kolahgar B, Geiss H, Möllmann-Coers M, Knaps A. 2000. The influence of valley winds on transport and dispersion of airborne pollutants in the Freiburg-Schauinsland area. *J. Geophys. Res.* **105**(D1): 1585–1597.

Kalthoff N, Adler B, Barthlott C, Corsmeier U, Mobbs S, Crewell S, Träumner K, Kottmeier C, Wieser A, Smith V. 2009. The impact of convergence zones on the initiation of deep convection: a case study from COPS. *Atmos. Res.* **93**: 680–694.

Kossmann M, Fiedler F. 2000. Diurnal momentum budget analysis of thermally induced slope wind. *Meteorol. Atmos. Phys.* **75**: 195–215.

Kossmann M, Vogtlin R, Corsmeier U, Vogel B, Fiedler F, Binder H, Kalthoff N, Beyrich F. 1999. Observations of handover processes between the atmospheric boundary layer and the free troposphere over mountainous terrain. *Contrib. Atmos. Phys.* **72**: 329–350.

Kottmeier C, Kalthoff N, Barthlott C, Corsmeier U, Van Baelen J, Behrendt A, Behrendt R, Blyth A, Coulter R, Crewell S, Di Girolamo P, Dorninger M, Flamant C, Foken T, Hagen M, Hauck C, Höller H, Konow H, Kunz M, Mahlke H, Mobbs SD, Richard E, Steinacker R, Weckwerth TM, Wieser A, Wulfmeyer V. 2008. Mechanisms initiating

deep convection over complex terrain during COPS. *Meteorol. Z.* **17**: 931–948.

Meissner C, Kalthoff N, Kunz M, Adrian G. 2008. Initiation of shallow convection in the Black Forest mountains. *Atmos. Res.* **86**: 42–60.

Radlach M, Behrendt A, Wulfmeyer V. 2008. Scanning rotational Raman lidar at 355 nm for the measurement of tropospheric temperature fields. *Atmos. Chem. Phys.* **8**: 159–169.

Raymond DJ, Wilkening M. 1980. Mountain-induced convection under fair weather conditions. *J. Atmos. Sci.* **37**: 2693–2706.

Raymond D, Wilkening M. 1982. Flow and mixing in New Mexico mountain cumuli. *J. Atmos. Sci.* **39**: 2211–2228.

Rotach MW, Ambrosetti P, Ament F, Appenzeller C, Arpagaus M, Bauer H-S, Behrendt A, Bouttier F, Buzzi A, Corazza M, Davolio S, Denhard M, Dorninger M, Fontannaz L, Frick J, Fundel F, Germann U, Gorgas T, Hegg C, Hering A, Keil C, Liniger MA, Marsigli C, McTaggart-Cowan R, Montani A, Mylne K, Ranzi R, Richard E, Rossa A, Santos-Muñoz D, Schär C, Seity Y, Staudinger M, Stoll M, Volkert H, Walser A, Wang Y, Werhahn J, Wulfmeyer V, Zappa M. 2009a. MAP D-PHASE: Real-time demonstration of weather forecast quality in the Alpine region. *Bull. Am. Meteorol. Soc.* **90**: 1321–1336.

Rotach MW, Ambrosetti P, Ament F, Appenzeller C, Arpagaus M, Bauer H-S, Behrendt A, Bouttier F, Buzzi A, Corazza M, Davolio S, Denhard M, Dorninger M, Fontannaz L, Frick J, Fundel F, Germann U, Gorgas T, Hegg C, Hering A, Keil C, Liniger MA, Marsigli C, McTaggart-Cowan R, Montani A, Mylne K, Ranzi R, Richard E, Rossa A, Santos-Muñoz D, Schär C, Seity Y, Staudinger M, Stoll M, Volkert H, Walser A, Wang Y, Werhahn J, Wulfmeyer V, Zappa M. 2009b. Supplement: Additional applications of the D-PHASE data sets. *Bull. Am. Meteorol. Soc.* **90**: (electronic supplement) 28–32.

Skamarock WC, Klemp JB, Dudhia J, Gill DO, Barker DM, Duda MG, Huang X, Wang W, Powers JG. 2008. '*A description of the Advanced Research WRF Version 3*', Technical Report NCAR/TN-475+STR. National Center for Atmospheric Research: Boulder, CO.

Weckwerth TM, Wilson JW, Hagen M, Emerson TJ, Grebe L. 2011. Radar climatology of the COPS region. *Q. J. R. Meteorol. Soc.* **137**(S1): 31–41.

Weisman ML, Davis C, Wang W, Manning KW, Klemp JB. 2008. Experiences with 0–36-h explicit convective forecasts with the WRF-ARW model. *J. Atmos. Sci.* **43**: 407–437.

Whiteman CD. 2000. *Mountain Meteorology: Fundamentals and Applications.* Oxford University Press: Oxford, UK.

Whiteman DN. 2003. Examination of the traditional Raman lidar technique. II. Evaluating the ratios for water vapor and aerosols. *Appl. Opt.* **42**: 2593–2608.

Whiteman DN, Demoz B, Di Girolamo P, Comer J, Veselovskii I, Evans K, Wang Z, Sabatino D, Schwemmer G, Gentry B, Lin R-F, Behrendt A, Wulfmeyer V, Browell E, Ferrare R, Ismail S, Wang J. 2006. Raman Water Vapor Lidar Measurements During the International H_2O Project. II. Case Studies. *J. Atmos. Oceanic Technol.* **23**: 170–183.

Wulfmeyer V, Behrendt A, Adrian G, Althausen D, Aoshima F, van Baelen J, Barthlott C, Bauer H-S, Blyth A, Brandau C, Corsmeier U, Craig G, Crewell S, Dick G, Dorninger M, Dufournet Y, Ehret G, Engelmann R, Flamant C, Foken T, Di Girolamo P, Grassl H, Grzeschik M, Handwerker J, Hagen M, Hardesty RM, Hauck C, Junkermann W, Kalthoff N, Kiemle C, Kottmeier C, Krauss L, Long C, Lelieveld J, Madonna F, Miller M, Mobbs S, Neininger B, Pal S, Peters G, Radlach M, Richard E, Rotach M, Russchenberg H, Schluessel P, Schumann U, Simmer C, Steinacker R, Turner D, Vogt S, Volkert H, Weckwerth T, Wernli H, Wieser A, Wunraum C. 2007. The Convective and Orographically-induced Precipitation study (COPS): COPS Field Report 2.1. 368 pp. University of Hohenheim: Stuttgart, Germany.

Wulfmeyer V, Behrendt A, Bauer HS, Kottmeier C, Corsmeier U, Blyth A, Craig G, Schumann U, Hagen M, Crewell S, Di Girolamo P, Flamant C, Miller M, Montani A, Mobbs S, Richard E, Rotach MW, Arpagaus M, Russchenberg H, Schlüssel P, König M, Gärtner V, Steinacker R, Dorninger M, Turner DD, Weckwerth T, Hense A, Simmer C. 2008. The Convective and Orographically-induced Precipitation study: A research and development project of the world weather research program for improving quantitative precipitation forecasting in low-mountain regions. *Bull. Am. Meteorol. Soc.* **89**: 1477–1486.

Wulfmeyer V, Behrendt A, Kottmeier C, Corsmeier U, Barthlott C, Craig G, Hagen M, Althausen D, Aoshima F, Arpagaus M, Bauer H-S, Bennett L, Blyth A, Brandau C, Champollion C, Crewell S, Dick G, Di Girolamo P, Dorninger M, Dufournet Y, Eigenmann R, Engelmann R, Flamant C, Foken T, Gorgas T, Grzeschik M, Handwerker J, Hauck C, Hoeller C, Junkermann W, Kalthoff N, Kiemle C, Klink S, Koenig M, Krauss L, Long CN, Madonna F, Mobbs S, Neininger B, Pal S, Peters G, Pigeon G, Richard E, Rotach MW, Russchenberg H, Schwitalla T, Smith V, Steinacker R, Trentmann J, Turner DT, van Baelen J, Vogt S, Volkert H, Weckwerth T, Wernli H, Wieser A, Wirth M. 2011. The Convective and Orographically-induced Precipitation study (COPS): The scientific strategy, the field phase, and research highlights. *Q. J. R. Meteorol. Soc.* **137**(S1): 3–30, DOI: 10.1002/qj.752.

Wurman J, Straka J, Rasmussen E, Randall M, Zahrai A. 1997. Design and deployment of a portable, pencil-beam, pulsed, 3-cm Doppler radar. *J. Atmos. Oceanic Technol.* **14**: 1502–1512.

